Corrosion Behavior of NiTi Alloys Fabricate by Selective Laser Melting Subjected to Femtosecond Laser Shock Peening

Long Ma [1], Wanqing Li [1], Yongzhi Yang [1], Yuanxue Ma [1], Kai Luo [1], Bochao Jia [2], Zezhou Xu [3,*] and Zhenglei Yu [3,*]

1   Aviation Operations Service College, Aviation University of Air Force, Changchun 130022, China; chenlixin985@163.com (L.M.); 17843121301@163.com (W.L.); Z17852031954@163.com (Y.Y.); lilunxin@mails.cust.edu.cn (Y.M.); Ytguo@jlu.edu.cn (K.L.)
2   College of Mechanical and Electric Engineering, Changchun University of Science and Technology, Changchun 130022, China; jiabochao1122@163.com
3   Key Lab of Bionic Engineering, Ministry of Education, Jilin University, Changchun 130000, China
*   Correspondence: zzxu20@mails.jlu.edu.cn (Z.X.); zlyu@jlu.edu.cn (Z.Y.)

Abstract: NiTi alloys are commonly used in many fields such as aerospace, mechanical engineering due to their excellent mechanical properties and shape memory effect. In recent years, the emergence of selective laser melting (SLM) technology provides a new method for the preparation of NiTi parts. But the surface corrosion failure of SLM-NiTi is the most common problem. This paper mainly focuses on the research of femtosecond laser shock peening of the surface of SLM-NiTi alloy to improve the corrosion resistance. Selecting different scanning space (1 μm, 3 μm, 5 μm, 10 μm), and analyze the surface morphology of the material through the OM, SEM, EDS and white light interferometer, and investigate the surface nanohardness and corrosion resistance through nanoindentation and electrochemical testing. The research results show that part of the TiO_2 is formed under different scanning spaces, and part of NiO is formed when the scanning space is 1μm. At the same time, it is found that the sample under the condition of 10 μm has the most excellent corrosion resistance and nanohardness. The nanohardness reaches 1303 ± 40 HV and the corrosion current density reaches $1.45 \pm 0.1 \times 10^{-9}$ A·cm^{-2}. Proper femtosecond laser treatment can effectively improve the surface strength and corrosion resistance of the NiTi alloys.

Keywords: NiTi alloys; femtosecond laser; shock peening; corrosion behavior; selective laser melting

1. Introduction

NiTi alloy has excellent biocompatibility, excellent corrosion resistance, unique superelasticity (SE) and shape memory effects (SME), so it is widely used in many fields such as aerospace and biomedicine [1–4]. However, poor machinability and work hardening severely limit the application of NiTi alloy, which can only be processed into simple wires, bars and pipes, etc. [5–7]. Currently, additive manufacturing (AM) such as selective laser melting (SLM), electron beam melting (EBM), and directed energy deposition (DED) is the best method for for overcoming the problems [4,8,9]. Recently, we optimized the molding quality through orthogonal experiments and obtained the optimal process parameters and scanning strategy [10].

Additive manufacturing NiTi alloys are commonly used materials in aerospace, mechanical engineering, and biomedicine, and structural. However, the material failures caused by surface corrosion are inevitable. Therefore, enhancing surface property is the basis for the long-term use of additive manufacturing of NiTi [11–14]. Surface treatment is a commonly used method to improve surface corrosion resistance, such as laser cladding [15] and surface film [16]. With the development of nanotechnology, the establishment of surface nanostructures has become a new way to improve surface properties, especially nanosecond laser processing and femtosecond laser processing, commonly used for surface

treatment of stainless steel [17], titanium alloy [18], magnesium alloy [19] and aluminum alloy [20] etc.

Trdan et al. [21] studied the effect of femtosecond laser shock peening on the corrosion behavior of AA2024-T3, and it was found that the main reason for femtosecond laser peening to improve corrosion resistance may be the refined structure and the reduction of intergranular corrosion; Kolobov et al. [22] found that TiO_2, Ti_3O_5 and TiO were mainly generated after femtosecond laser treatment of Ti-6Al-4V surface; The nanosecond laser treatment of aluminum alloy surface reported by Boinovich et al. [23] effectively inhibited the occurrence of pitting corrosion. However, Femtosecond laser processing of NiTi surface has not yet been systematically studied. Only Wang et.al analyzed the friction resistance [24] and corrosion resistance [25] of NiTi alloy surface strengthened by femtosecond laser shock peening, and found that the femtosecond laser shock peening can help improve the properties of the NiTi alloy surface. But the effect of femtosecond laser parameters on the surface of NiTi alloy has not been studied, and the current studies on parameters are limited to stainless steel and aluminum alloys. Regarding the additive manufacturing of NiTi, no relevant research has been found either. As we all known, SLM in additive manufacturing technology is widely used in the processing of NiTi alloys [26–28]. However, there are still a series of questions on the surface of SLM-NiTi, such as the release of Ni^{2+} [12,29], and the corrosion behavior [30] relatively need to be improved. Therefore, it is feasible and necessary to improve the corrosion resistance of NiTi alloy surface by femtosecond laser surface treatment.

Through parameter design in the early stage, SLM-NiTi with excellent surface quality and excellent mechanical properties was obtained (Figure 1). In this paper, we selected different femtosecond laser scanning spaces for exploration (Table 1) and analyzed the trends of sample surface composition and corrosion resistance.
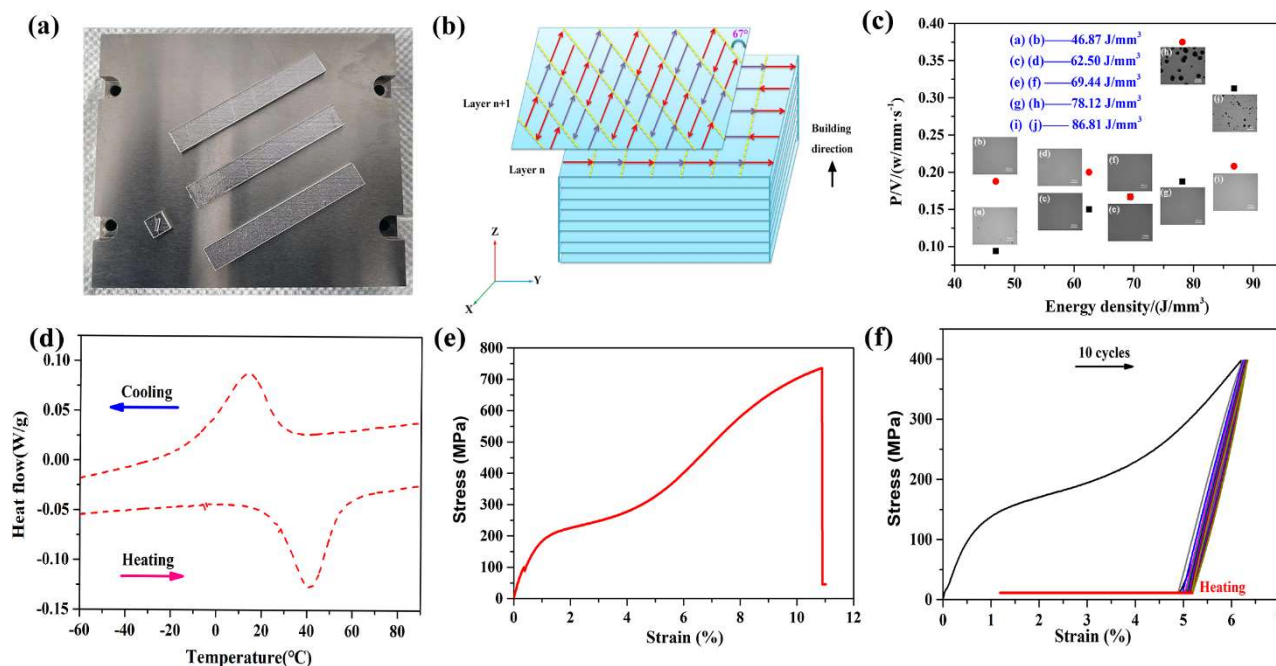
Figure 1. (**a**) 3D printing NiTi alloy samples; (**b**) Schematic diagram of printing strategy; (**c**) Surface forming quality of samples with different parameters under the optical microscope; (**d**) DSC curve; (**e**) Tensile fracture curve; (**f**) Heating recovery curve after ten cycles [10].

Table 1. Femtosecond laser parameter design.

Sample	Powder (w)	Scanning Speed (mm/s)	Frequency (kHz)	Scanning Space (μm)
1 μm	8	60	20	1
3 μm	8	60	20	3
5 μm	8	60	20	5
10 μm	8	60	20	10

2. Fabrication and Experimental Methods

2.1. Femtosecond Laser Shock Peening Experiments

The SLM-NiTi alloy prepared by the previous research was selected in this study. Before the experiment, the surface of each sample was polished with abrasive papers (using SiC paper 180# to 2000#), ultrasonic cleaning and alcohol wipe were performed. The femtosecond laser system (RAPID 10 Industrial Picosecond Laser System) was produced by the USA with wavelength 1064nm, pulse width 20 ± 5 ps, beam diameter 3 mm and direct spot 32–50 μm. All samples are selected with a power of 8 W, a scanning speed of 60 mm/s, and a frequency of 20 kHz, and different scanning distances, 10 μm, 5 μm, 3 μm, and 1 μm are selected respectively. And the processing schematic diagram is shown in Figure 2.
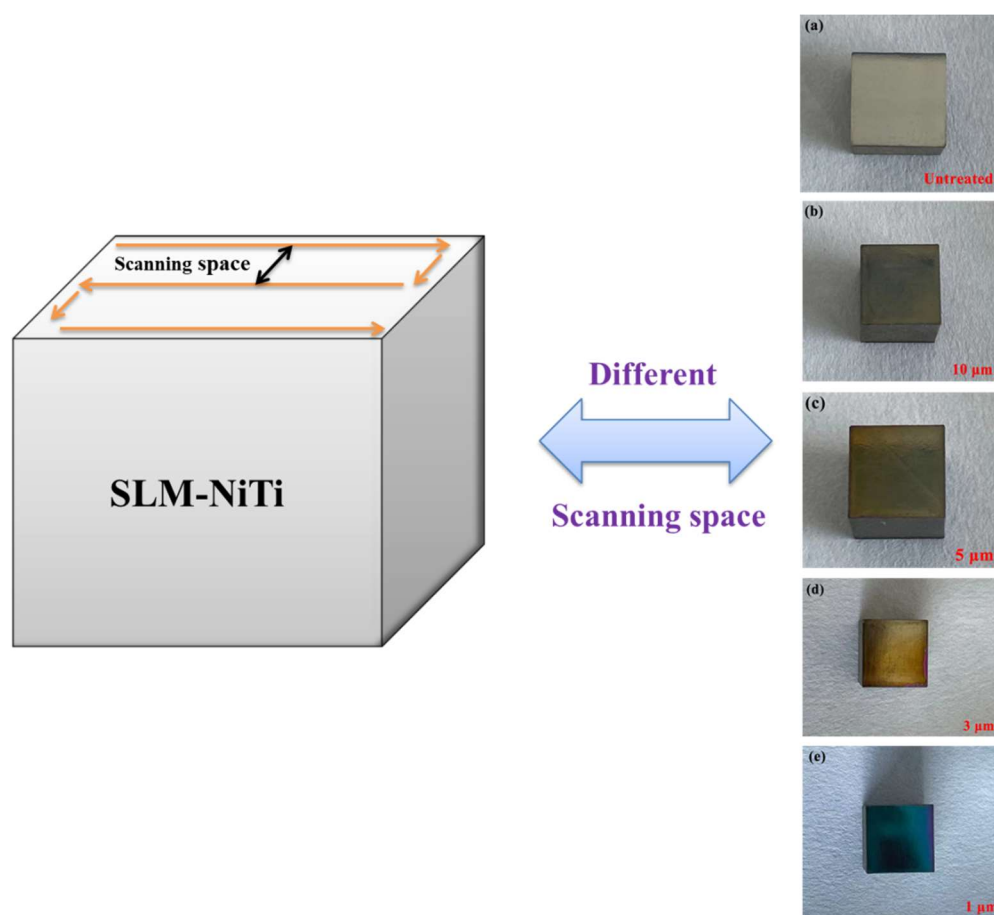
Figure 2. Schematic diagram of femtosecond laser processing path. (**a**) As-fabricated (**b**) 10 μm (**c**) 5 μm (**d**) 3 μm (**e**) 1 μm.

2.2. Test Methods

The optical microscope (OM, Zeiss AXIO, Oberkochen, Germany) and scanning electron microscope (SEM, ZEISS EV018, Oberkochen, Germany) equipped with energy dispersive spectroscopy (EDS, Oxford Instruments, Abingdon, UK) were used to the surface morphologies of the different samples. The white light interferometer was used to test the roughness and 3D images of sample surface. An X-Ray diffractometer (XRD, SHIMADZU XRD-7000, Shimadzu Scientific Instruments, Tokyo, Japan) with Cu Kα radiation operated at 40 kV and 30 mA was used to determine the phase composition. And the nanoindenter (Anton Paar Step-NHT3, Graz, Austria) was used to measure the nano-hardness, the indentation adopted a load of 20 mN, and pause 5 s, a frequency of 10.0 Hz.

The electrochemical polarization curves and electrochemical impedance spectroscopy (EIS) curves of HP and LP were carried out in 3.5 wt % NaCl at 25 ± 0.5 °C (RT) on the electrochemical station (VersaSTAT3, Princeton Applied Research, Oak Ridge, TN, USA). In the application of the three-electrode system and the electrochemical test, the reference electrode was a saturated calomel electrode (SCE), the counter-electrode is a platinum sheet with an area of 1 cm × 1 cm, and the working electrode was the tested sample. The sample was immersed in 3.5 wt% NaCl for 1 h before the experiment to ensure the stability of the open circuit potential (OCP). The EIS measurement was conducted at the OCP by applying a sinusoidal penitential of 10 mV in the frequency range from 10^5 to 10^{-2} Hz. And ZsimpWin (Version 3.60) software was used for fitting analysis. The potentiodynamic polarization curves were obtained from −1 to 1 V VS OCP with a scanning rate of 1 mV/s. The Tafel extrapolation method was used to obtain the values of corrosion current density (I_{corr}) and corrosion potential (E_{corr}). All the electrochemical tests were carried out three times for each condition.

3. Results

3.1. XRD Analysis

Figure 3 depicted the XRD pattern of SLM-NiTi alloys after femtosecond laser shock peening. It can be seen from that after the femtosecond laser, the TiO_2 was formed on the surface. This was mainly because after shock peening in the air, Ti combines with O to form TiO_2. Secondly, we found that the volume fraction of B19′NiTi increased significantly. This may be due to the fact that the melting point of Ni is lower than that of Ti, dissipating prior to Ti, and combining with O. This was why the 1μm sample (large remelting area and high surface temperature) could be seen more obvious NiO phase.
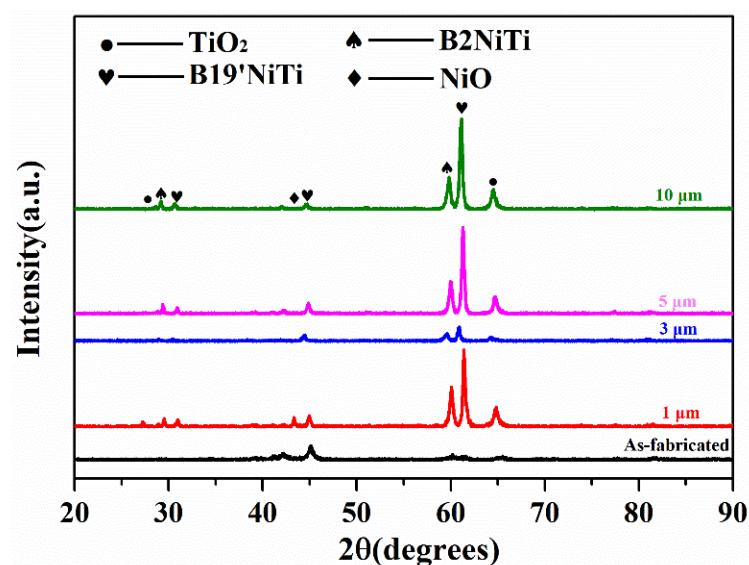

Figure 3. XRD patterns of different samples processed by femtosecond laser shock peening.

### 3.2. White Light Interference and Microstructure

Figure 4 showed the OM image of different samples. It could be found that the surface undergoes a femtosecond laser strengthening treatment with obvious discoloration reaction, which indicated the formation of new phase, and the products generated on the surface of different samples are not the same, especially the 1 μm sample, this is mainly caused by the TiO_2 or NiO produced. Figure 5 showed the SEM images and EDS analysis under different parameters. It can be found that the laser ablation spots on the surface after femtosecond laser processing were arranged in an orderly manner with a small number of unmelted particles which showed that the ablation layer is formed on the surface of NiTi alloy. This is the result of the interaction between the femtosecond pulsed laser beam and the NiTi alloy. At the same time, we found that the samples with scan spacing of 1 μm and 3 μm had cracks, which mainly because the scan spacing was small led to thermal stress concentration and cracking. EDS analysis was further carried out to analyze the surface composition. The content of Ni on the surface of the substrate was significantly reduced, and the content of Ti and O increased. This might be due to the formation of TiO_2 on the surface of NiTi alloy. Especially when the scanning distance is reduced to 1 μm, the Ni content increased significantly, which might be caused by the formation of NiO on the surface of the sample, which is consistent with the XRD analysis results. The surface roughness of processed samples was measured by white light interference (Figure 6). It was illustrated that femtosecond laser processing may increase surface roughness [17] which is mainly due to laser ablation and slight plastic deformation. And increasing the scanning distance would decrease the remelting area, leading to a decrease in surface roughness.
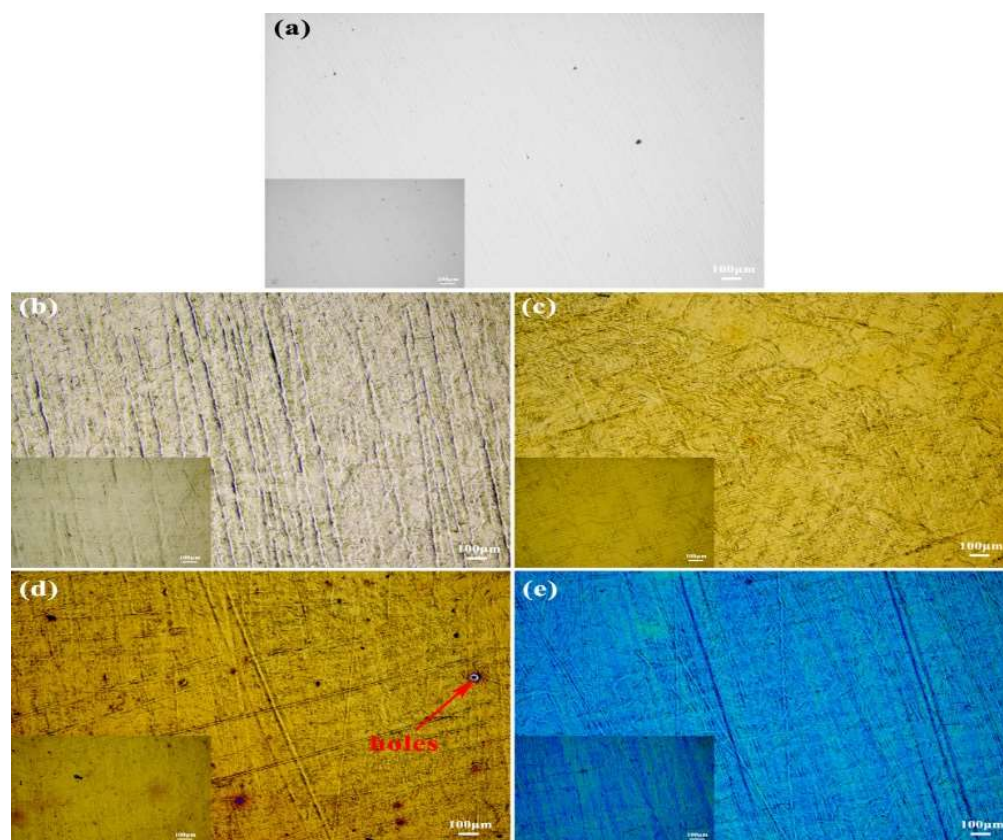
Figure 4. Surface morphologies of samples before and after femtosecond laser (**a**) As-fabricated (**b**) 10 μm (**c**) 5 μm (**d**) 3 μm (**e**) 1 μm.
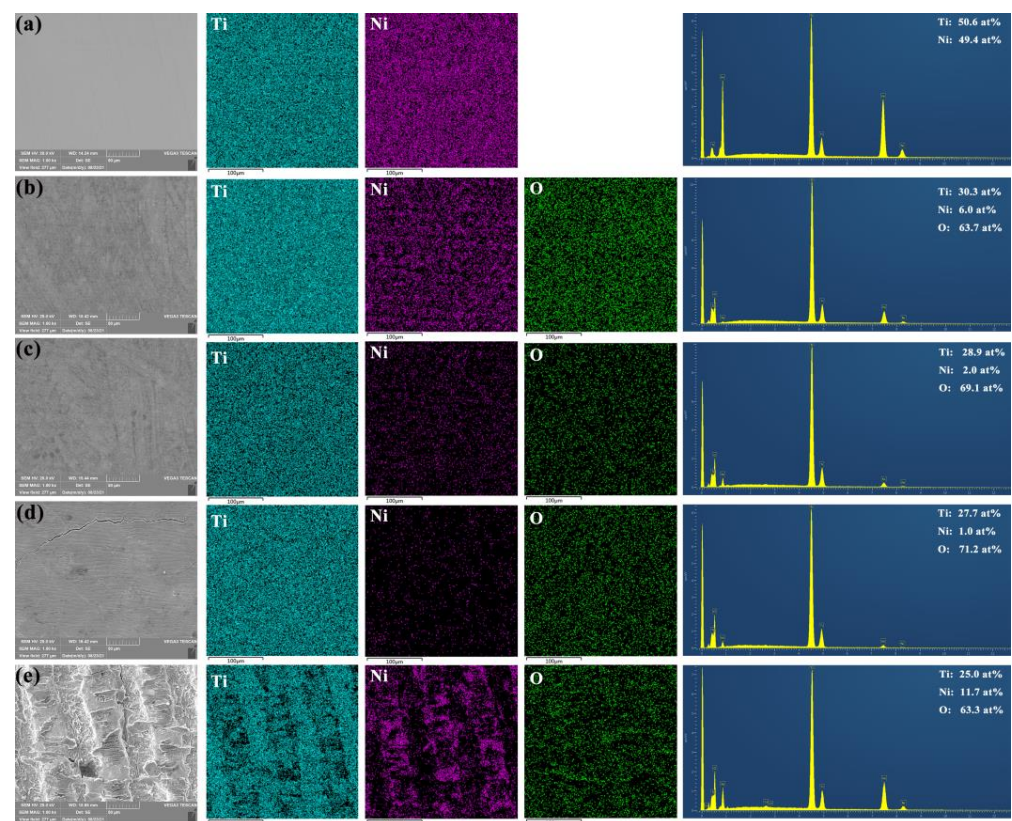
Figure 5. SEM image of samples before and after femtosecond laser (**a**) As-fabricated (**b**) 10 μm. (**c**) 5 μm (**d**) 3 μm (**e**) 1 μm.
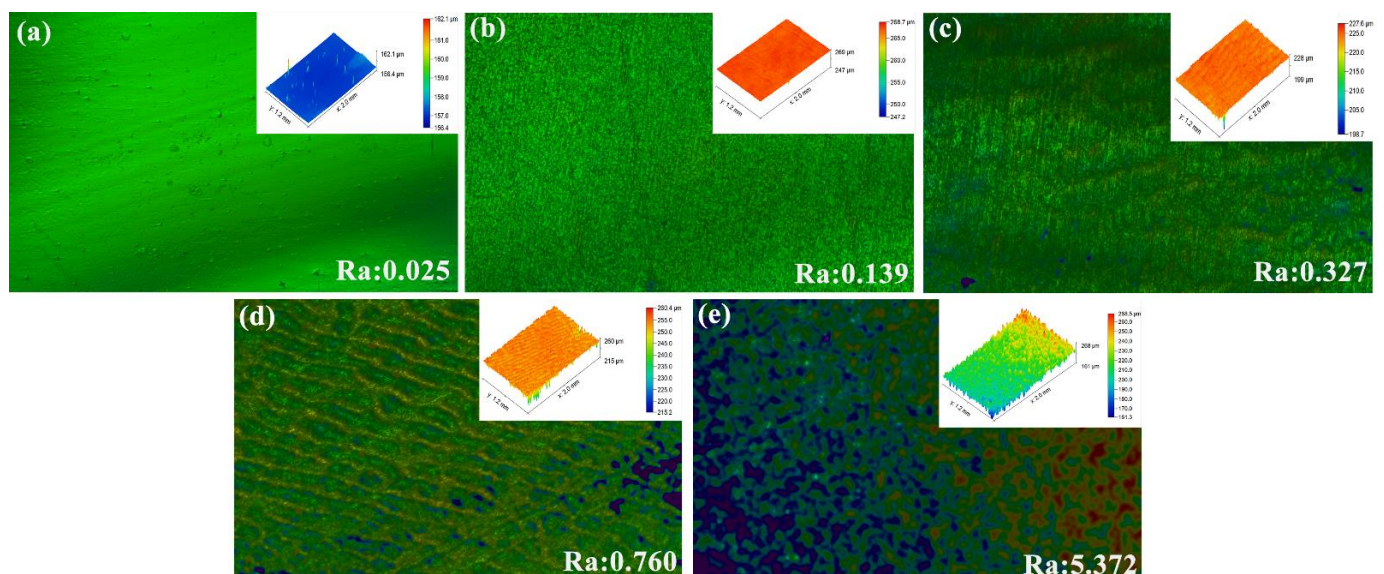
Figure 6. Surface optical images and surface roughness of different samples (**a**) As-fabricated; (**b**) 10 μm; (**c**) 5 μm; (**d**) 3 μm; (**e**) 1 μm.

3.3. Nanoindentation Hardness Analysis

Figure 7 showed the nano-hardness curve of the samples. Under the condition of 1 μm, due to the small scanning spacing, the surface of the sample was overburned and softened, which reduced the surface nano-hardness of the sample (206 ± 20 HV), while the surface grains of other samples were refined and the hardness increased due to femtosecond laser

processing. Simultaneously, the 10 µm sample exhibited the highest surface nano-hardness (1303 ± 40 HV), this is in line with the Hall-Petch formula [31], i.e., $\delta_s = \delta_i + k_s d^{-1}$. Where d is the crystal grain diameter, δ_s is the yield strength of the material, δ_i is the movement resistance of the dislocation in the base metal, and k_s is the crystal structure constant.
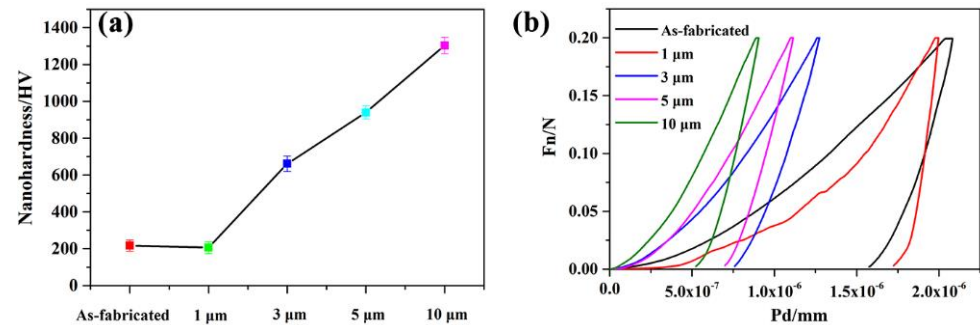
Figure 7. (**a**) Comparison of nano-hardness under different process parameters (**b**) Load-displacement curve of samples surface under different process parameters.

3.4. Electrochemical Corrosion Behavior

The potentiodynamic polarization curves of different samples were shown in Figure 8. Table 2 showed that the corrosion current density (I_{corr}) and corrosion potential (E_{corr}) obtained in the polarization curve. The I_{corr} always determined the corrosion resistance of the samples and showd the corrosion rate of the material in a corrosive medium. It can be found that the I_{corr} was the lowest under the condition of 10 µm, which is mainly because the formation of TiO_2 protects the substrate. But the sample surface of 1 µm and 3 µm is higher than the as-fabricated. This might be related to the shock peening effect caused by the scanning spacing, and the excessively large remelting area leads to the overburning of the sample surface (the overburning holes produced in Figure 4d). Simultaneously, the cracks produced by overburning at 1 µm and 3 µm in Figure 5 are also important factors affecting corrosion behavior.
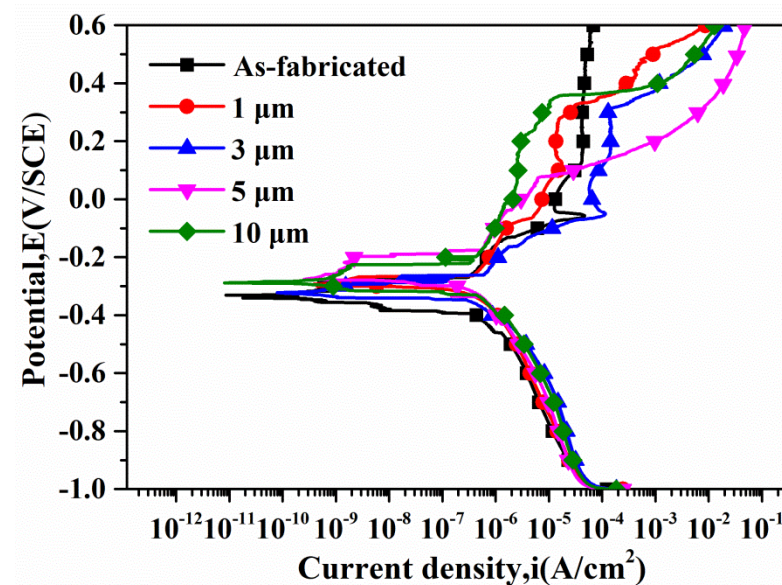
Figure 8. Polarization curves in 3.5 wt % NaCl solution under different process parameters.

Table 2. Corrosion parameters extracted from the Polarization curves.

Samples	B_a/mV	B_c/mV	E_{corr}/V	I_{corr}/A·cm^{-2}
As-fabricated	279.46 ± 2.5	169.68 ± 4.1	-0.32 ± 0.02	$1.00 \pm 0.2 \times 10^{-8}$
1 μm	56.86 ± 2.1	78.77 ± 2.5	-0.29 ± 0.04	$4.95 \pm 0.3 \times 10^{-8}$
3 μm	61.43 ± 1.3	74.15 ± 3.3	-0.31 ± 0.08	$4.08 \pm 1.1 \times 10^{-7}$
5 μm	66.19 ± 2.2	81.98 ± 2.5	-0.24 ± 0.03	$1.97 \pm 0.3 \times 10^{-9}$
10 μm	74.71 ± 2.3	71.53 ± 3.4	-0.27 ± 0.05	$1.67 \pm 0.1 \times 10^{-9}$

The corrosion behavior of the SLM-NiTi and different scanning space samples in the 3.5 wt % NaCl solution was further studied via EIS measurements (as shown in Figure 9). It was worth noting that the 10 μm sample showed the largest loop than the others, had the highest value of low-frequency impedance modulus i.e., |Z| value, and the phase angles at the medium frequency range of 10 μm was the highest, which means that best corrosion protection performance [32,33].
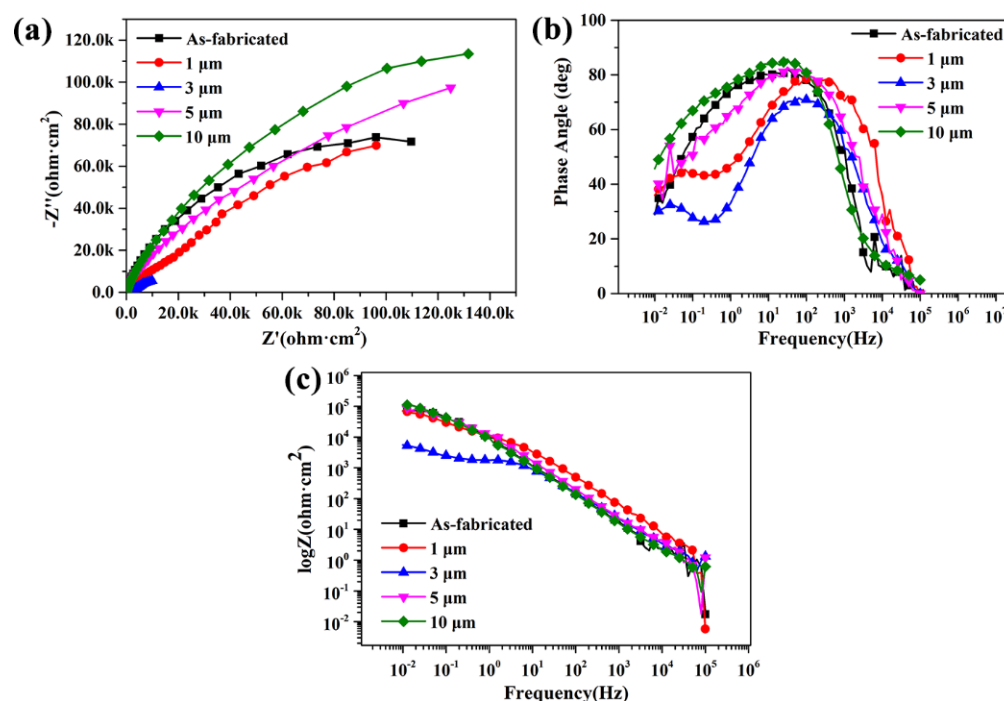
Figure 9. EIS of the different samples (**a**) Nyquist curves (**b**) Bode phase (**c**) Bode impedance.

To more accurately explain the results of EIS in detail, the equivalent electrical circuits are shown in Figure 10. The fitting results were shown in Table 3, in which R_s represents the solution resistance; CPE-film is used instead of a pure capacitive, which is defined by admittance (Y_0) and power index number (n), and can be calculated by the formula ($Y_{CPE}(\omega) = 1/Z_{CPE} = Y_0(j\omega)^n$) [34]. R_p represents charge transfer resistance. Under the condition of 10μm, it had the smallest CPE-film value and a largest R_p value, where the CPE-film value was related to the corrosion area [35]. At the same time, the value of R_p was positively correlated with corrosion resistance [32], indicating that it had the best corrosion resistance under the condition of 10 μm, which was consistent with the results obtained by the polarization curve and EIS. Refinement of grain size might be the main reason for improving corrosion resistance, the crystal grains were remarkably refined, enabling the passivation film to be easily formed at the grain boundary by reducing the Cl- diffusion in the solution. However, the difference in surface roughness also affected the corrosion behavior of the material surface. Rough sample surfaces are more likely to form corrosion sites, which will cause corrosion. The increase of the scanning distance leads to a smaller surface roughness, which further improves the corrosion resistance.
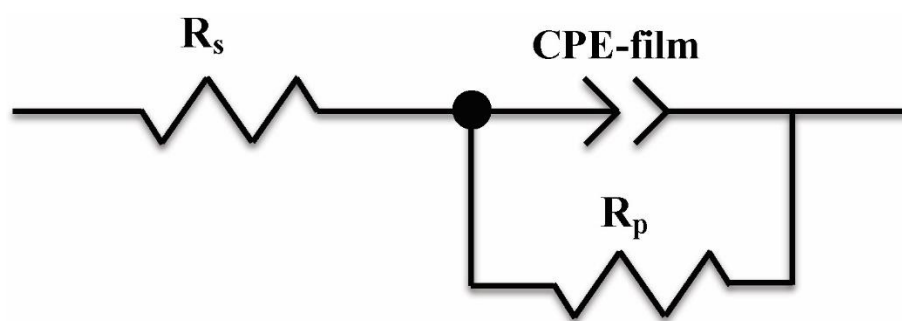
Figure 10. Equivalent circuit used to fit the data.

Table 3. Fitting results of the electrochemical parameters from EIS plots.

Samples	R_s ($\Omega\cdot cm^2$)	CPE-film	R_p ($\Omega\cdot cm^2$)	n
As-fabricated	57.11 ± 2.5	$(2.168 \pm 0.3) \times 10^{-5}$	$(1.873 \pm 0.4) \times 10^5$	0.8412 ± 0.04
1 μm	56.23 ± 3.5	$(2.302 \pm 0.2) \times 10^{-5}$	$(1.285 \pm 0.3) \times 10^5$	0.8008 ± 0.03
3 μm	51.17 ± 4.8	$(2.779 \pm 0.5) \times 10^{-5}$	$(1.685 \pm 0.2) \times 10^4$	0.7187 ± 0.01
5 μm	48.24 ± 2.7	$(1.681 \pm 0.4) \times 10^{-5}$	$(2.439 \pm 0.5) \times 10^5$	0.8596 ± 0.03
10 μm	53.18 ± 2.3	$(1.365 \pm 0.3) \times 10^{-5}$	$(3.439 \pm 0.4) \times 10^5$	0.8865 ± 0.05

4. Conclusions

This paper mainly studied the effect of femtosecond laser processing on the corrosion resistance of SLM-NiTi, mainly focusing on the effect of scanning space on the performance, and the conclusions are as follow:

(1) The scanning distance will affect the phase composition and surface roughness at the same time. After the femtosecond laser, the TiO_2 was mainly generated. When the scanning space was too small (1 μm), part of NiO was generated. The reduction of the scanning distance will result in an increase in surface roughness.

(2) Femtosecond laser shock peening could effectively increase the nanohardness of the material, and the nanohardness of the 10 μm sample was the highest, which can reach 1303 ± 40 HV. However, if the scanning distance is too small (1 μm), the hardness will be significantly reduced.

(3) The sample under the condition of scanning distance of 10 μm exhibited the most excellent corrosion resistance, and the I_{corr} could reach $1.45 \pm 0.1 \times 10^{-9}$ A·cm^{-2}. The grain refinement after femtosecond laser processing may be the main reason that affects the hardness and corrosion resistance.

Author Contributions: L.M.: literature search, study design, data analysis. W.L.: literature search, figures, study design, data collection. Y.Y.: data analysis, data interpretation, writing, data collection. Y.M.: study design, data analysis, figures. K.L.: literature search, study design, data analysis. B.J.: data collection, figures, study design. Z.X.: study design, data analysis, writing. Z.Y.: study design, data analysis, writing. All authors have read and agreed to the published version of the manuscript.

References

1. Zhao, M.; Shao, Y.; Zheng, W.; Luo, Y.; Qiao, J.; Wu, S.; Yan, Y.; Guo, W. Tailoring the damping and mechanical properties of porous NiTi by a phase leaching process. *J. Alloys Compd.* **2021**, *855*, 157471. [CrossRef]
2. Yu, H.; Qiu, Y.; Young, M.L. Influence of Ni4Ti$_3$ precipitate on pseudoelasticity of austenitic NiTi shape memory alloys deformed at high strain rate. *Mater. Sci. Eng. A* **2021**, *804*, 140753. [CrossRef]
3. Zhang, Q.; Hao, S.; Liu, Y.; Xiong, Z.; Guo, W.; Yang, Y.; Ren, Y.; Cui, L.; Ren, L.; Zhang, Z. The microstructure of a selective laser melting (SLM)-fabricated NiTi shape memory alloy with superior tensile property and shape memory recoverability. *Appl. Mater. Today* **2020**, *19*, 100547. [CrossRef]
4. Elahinia, M.; Moghaddam, N.S.; Andani, M.T.; Amerinatanzi, A.; Bimber, B.A.; Hamilton, R.F. Fabrication of NiTi through additive manufacturing: A review. *Prog. Mater. Sci.* **2016**, *83*, 630–663. [CrossRef]
5. Saedi, S.; Turabi, A.S.; Andani, M.T.; Haberland, C.; Elahinia, M.; Karaca, H. Thermomechanical characterization of Ni-rich NiTi fabricated by selective laser melting. *Smart Mater. Struct.* **2016**, *25*, 035005. [CrossRef]
6. Wang, C.; Tan, X.; Du, Z.; Chandra, S.; Sun, Z.; Lim, C.; Tor, S.B.; Wong, C. Additive manufacturing of NiTi shape memory alloys using pre-mixed powders. *J. Mater. Process. Technol.* **2019**, *271*, 152–161. [CrossRef]
7. Yan, Y.X.; Ahmad, T.; Zhang, X.; Liang, T.; Rehman, S.U.; Manzoor, M.U.; Liu, W.; Basit, M.A.; Saim, A.B. Microstructure, hardness and corrosion behavior of Ni-Ti alloy with the addition of rare earth metal oxide (Gd$_2$O$_3$). *Mater. Res. Express* **2019**, *6*, 076513. [CrossRef]
8. Khoo, Z.X.; Liu, Y.; An, J.; Chua, C.K.; Shen, Y.F.; Kuo, C.N. A review of selective laser melted NiTi shape memory alloy. *Materials* **2018**, *11*, 519. [CrossRef]
9. Chen, X.; Liu, K.; Guo, W.; Gangil, N.; Siddiquee, A.N.; Konovalov, S. The fabrication of NiTi shape memory alloy by selective laser melting: A review. *Rapid Prototyp. J.* **2019**, *25*, 1421–1432. [CrossRef]
10. Yu, Z.; Xu, Z.; Guo, Y.; Xin, R.; Liu, R.; Jiang, C.; Li, L.; Zhang, Z.; Ren, L. Study on properties of SLM-NiTi shape memory alloy under the same energy density. *J. Mater. Res. Technol.* **2021**, *13*, 241–250. [CrossRef]
11. Saugo, M.; Flamini, D.O.; Saidman, S.B. Low-voltage polarization in AOT Solution to enhance the corrosion resistance of nitinol. *J. Mater. Eng. Perform.* **2021**, *30*, 1816–1824. [CrossRef]
12. Veverkova, J.; Bartkova, D.; Weiser, A.; Dlouhy, A.; Babula, P.; Štěpka, P.; Goldbergova, M.P. Effect of Ni ion release on the cells in contact with NiTi alloys. *Environ. Sci. Pollut. Res.* **2020**, *27*, 7934–7942. [CrossRef]
13. Velmurugan, C.; Senthilkumar, V.; Kamala, P.S. Microstructure and corrosion behavior of NiTi shape memory alloys sintered in the SPS process. *Int. J. Miner. Met. Mater.* **2019**, *26*, 1311–1321. [CrossRef]
14. Qiu, P.; Gao, P.; Wang, S.; Li, Z.; Yang, Y.; Zhang, Q.; Xiong, Z.; Hao, S. Study on corrosion behavior of the selective laser melted NiTi alloy with superior tensile property and shape memory effect. *Corros. Sci.* **2020**, *175*, 108891. [CrossRef]
15. Yuan, W.; Li, R.; Chen, Z.; Gu, J.; Tian, Y. A comparative study on microstructure and properties of traditional laser cladding and high-speed laser cladding of Ni45 alloy coatings. *Surf. Coat. Technol.* **2021**, *405*, 126582. [CrossRef]
16. Wang, L.; Chen, M.; Liu, H.; Jiang, C.; Ji, V.; Moreira, F. Optimisation of microstructure and corrosion resistance of Ni-Ti composite coatings by the addition of CeO$_2$ nanoparticles. *Surf. Coat. Technol.* **2017**, *331*, 196–205. [CrossRef]
17. Nishimura, A.; Minehara, E.; Tsukada, T.; Kikuchi, M.; Nakano, J. Ablation of work hardening layers against stress corrosion cracking of stainless steel by repetitive femtosecond laser pulses. In *Fifth International Symposium on Laser Precision Microfabrication*; Miyamoto, I., Helvajian, H., Itoh, K., Kobayashi, K.F., Ostendorf, A., Sugioka, K., Eds.; International Society for Optics and Photonics: Bellingham, WA, USA, 2004; pp. 673–677.
18. Jeong, Y.-H.; Kim, W.-G.; Choe, H.-C. Electrochemical behavior of nano and femtosecond laser textured titanium alloy for implant surface modification. *J. Nanosci. Nanotechnol.* **2011**, *11*, 1581–1584. [CrossRef]
19. Park, J.; Han, H.-S.; Park, J.; Seo, H.; Edwards, J.; Kim, Y.-C.; Ok, M.-R.; Seok, H.-K.; Jeon, H. Corrosion behavior of biodegradable Mg-based alloys via femtosecond laser surface melting. *Appl. Surf. Sci.* **2018**, *448*, 424–434. [CrossRef]
20. Kawashima, T.; Sano, T.; Hirose, A.; Tsutsumi, S.; Masaki, K.; Arakawa, K.; Hori, H. femtosecond laser peening of friction stir welded 7075-T73 aluminum alloys. *J. Mater. Process. Technol.* **2018**, *262*, 111–122. [CrossRef]
21. Trdan, U.; Sano, T.; Klobčar, D.; Sano, Y.; Grum, J.; Šturm, R. Improvement of corrosion resistance of AA2024-T3 using femtosecond laser peening without protective and confining medium. *Corros. Sci.* **2018**, *143*, 46–55. [CrossRef]
22. Kolobov, Y.R.; Zhidkov, M.V.; Golosov, E.V.; Vershinina, T.; Kudryashov, S.I.; Makarov, S.V.; Ionin, A.A.; Ligachev, A.E. Phase composition and structure of femtosecond laser-produced oxide layer on VT6 alloy surface. *Laser Phys. Lett.* **2016**, *13*, 76103. [CrossRef]
23. Boinovich, L.B.; Emelyanenko, A.M.; Modestov, A.; Domantovsky, A.G.; Emelyanenko, K.A. Synergistic effect of superhydrophobicity and oxidized layers on corrosion resistance of aluminum alloy surface textured by nanosecond laser treatment. *ACS Appl. Mater. Interfaces* **2015**, *7*, 19500–19508. [CrossRef] [PubMed]
24. Wang, H.; Gurevich, E.L.; Ostendorf, A. Microhardness and microabrasion behaviour of NiTi shape memory alloy after femtosecond laser shock peening without coating in air. In *High-Power Laser Materials Processing: Applications, Diagnostics, and Systems IX*; Kaierle, S., Heinemann, S.W., Eds.; International Society for Optics and Photonics: Bellingham, WA, USA, 2020; Volume 11273, p. 1127301. [CrossRef]
25. Wang, H.; Jürgensen, J.; Decker, P.; Hu, Z.; Yan, K.; Gurevich, E.; Ostendorf, A. Corrosion behavior of NiTi alloy subjected to femtosecond laser shock peening without protective coating in air environment. *Appl. Surf. Sci.* **2020**, *501*, 144338. [CrossRef]

26. Zhang, C.; Zhu, J.; Zheng, H.; Li, H.; Liu, S.; Cheng, G. A review on microstructures and properties of high entropy alloys manufactured by selective laser melting. *Int. J. Extrem. Manuf.* **2020**, *2*, 032003. [CrossRef]

27. Yang, Y.; Zhan, J.; Sui, J.; Li, C.; Yang, K.; Castany, P.; Gloriant, T. Functionally graded NiTi alloy with exceptional strain-hardening effect fabricated by SLM method. *Scr. Mater.* **2020**, *188*, 130–134. [CrossRef]

28. Biffi, C.A.; Fiocchi, J.; Valenza, F.; Bassani, P.; Tuissi, A. selective laser melting of NiTi shape memory alloy: Processability, microstructure, and superelasticity. *Shape Mem. Superelasticity* **2020**, *6*, 342–353. [CrossRef]

29. Ibrahim, H.; Jahadakbar, A.; Dehghan, A.; Moghaddam, N.S.; Amerinatanzi, A.; Elahinia, M. In vitro corrosion assessment of additively manufactured porous NiTi structures for bone fixation applications. *Metals* **2018**, *8*, 164. [CrossRef]

30. Norouzi, N.; Nouri, Z. The effect of two-stage acid treatment on surface behavior and improvement of bioactivity of nitinol alloy. *Biointerface Res. Appl. Chem.* **2021**, *11*, 10690–10702.

31. Zhao, T.; Cai, X.; Wang, S.X.; Zheng, S. Effect of CeO_2 on microstructure and corrosive wear behavior of laser-cladded Ni/WC coating. *Thin Solid Films* **2000**, *379*, 128–132.

32. Guo, Y.; Jia, S.; Qiao, L.; Su, Y.; Gu, R.; Li, G.; Lian, J. Enhanced corrosion resistance and biocompatibility of poly-dopamine/dicalcium phosphate dihydrate/collagen composite coating on magnesium alloy for orthopedic applications. *J. Alloys Compd.* **2019**, *817*, 152782. [CrossRef]

33. Su, Y.; Lu, C.; Hu, X.; Guo, Y.; Xun, X.; Zhang, Z.; Li, G.; Lian, J.; Ren, L. Improving the degradation resistance and surface biomineralization ability of calcium phosphate coatings on a biodegradable magnesium alloy via a sol-gel spin coating method. *J. Electrochem. Soc.* **2018**, *165*, C155–C161. [CrossRef]

34. Guo, Y.; Su, Y.; Jia, S.; Sun, G.; Gu, R.; Zhu, D.; Li, G.; Lian, J. Hydroxyapatite/titania composite coatings on biodegradable magnesium alloy for enhanced corrosion resistance, cytocompatibility and antibacterial properties. *J. Electrochem. Soc.* **2018**, *165*, C962–C972. [CrossRef]

35. Huang, Y.S.; Zeng, X.T.; Hu, X.F.; Liu, F.M. Heat treatment effects on EN-PTFE-SiC composite coatings. *Surf. Coat. Technol.* **2005**, *198*, 173–177. [CrossRef]